

Frontier Molecular Orbital Contributions to Chlorination versus Hydroxylation Selectivity in the Non-Heme Iron Halogenase SyrB2

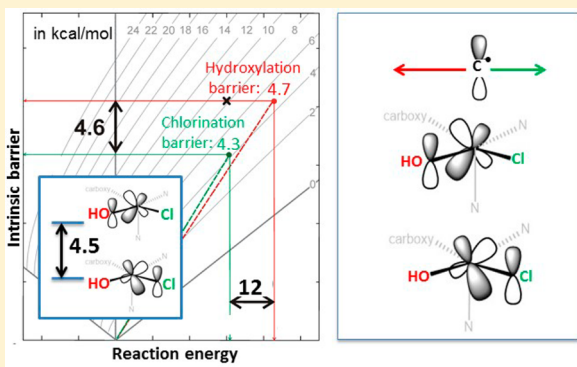
Martin Srnec^{*,‡,ID} and Edward I. Solomon^{*,†}

[†]Department of Chemistry, Stanford University, Stanford, California 94305-5080, United States

[‡]J. Heyrovský Institute of Physical Chemistry, The Czech Academy of Sciences, Dolejškova 2155/3, 182 23 Prague 8, Czech Republic

Supporting Information

ABSTRACT: The ability of an $\text{Fe}^{\text{IV}}=\text{O}$ intermediate in SyrB2 to perform chlorination versus hydroxylation was computationally evaluated for different substrates that had been studied experimentally. The π -trajectory for H atom abstraction ($\text{Fe}^{\text{IV}}=\text{O}$ oriented perpendicular to the C–H bond of substrate) was found to lead to the $S = 2$ five-coordinate $\text{HO}-\text{Fe}^{\text{III}}-\text{Cl}$ complex with the C^\bullet of the substrate, π -oriented relative to both the Cl^- and the OH^- ligands. From this ferric intermediate, hydroxylation is thermodynamically favored, but chlorination is intrinsically more reactive due to the energy splitting between two key redox-active $d\pi^*$ frontier molecular orbitals (FMOs). The splitting is determined by the differential ligand field effect of Cl^- versus OH^- on the Fe center. This makes chlorination effectively competitive with hydroxylation. Chlorination versus hydroxylation selectivity is then determined by the orientation of the substrate with respect to the $\text{HO}-\text{Fe}-\text{Cl}$ plane that controls either the Cl^- or the OH^- to rebound depending on the relative π -overlap with the substrate C radical. The differential contribution of the two FMOs to chlorination versus hydroxylation selectivity in SyrB2 is related to a reaction mechanism that involves two asynchronous transfers: electron transfer from the substrate radical to the iron center followed by late ligand (Cl^- or OH^-) transfer to the substrate.

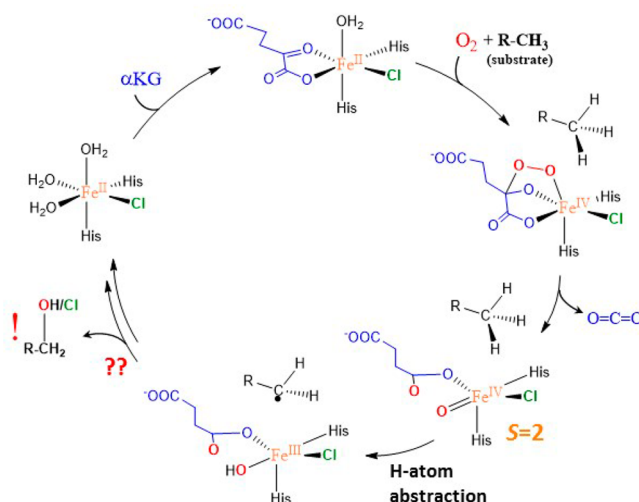


1. INTRODUCTION

Mononuclear nonheme iron (NHFe) enzymes are crucial catalysts in many vital biological processes.^{1,2} Their high reactivity and selectivity toward chemical functionalization of unreactive C–H bonds have stimulated significant efforts from different fields of chemistry to elucidate their reaction mechanisms and the factors contributing to their enzymatic efficiency. One such NHFe enzyme is the chloride, O_2 , and α -ketoglutarate-dependent NHFe halogenase SyrB2.

SyrB2 was discovered in the biosynthetic pathway of the phytotoxin syringomycin E (top of Scheme 1).^{3,4} SyrB2 was found to catalyze chlorination of the native substrate L-threonine that is attached to a small acyl carrier protein (ACP) through its phosphopantetheine linker. As for other members of the NHFe family, SyrB2 activates dioxygen to generate a high-spin ($S = 2$) $\text{Fe}^{\text{IV}}=\text{O}$ intermediate that further abstracts an H atom from the C–H bond of the substrate for its subsequent functionalization (chlorination in SyrB2). The $\text{Fe}^{\text{IV}}=\text{O}$ intermediate in SyrB2 was trapped and characterized using Mössbauer, Fe K-edge XAS, and EXAFS spectroscopies.⁵ The geometric structure of this intermediate was later defined using nuclear vibrational resonance spectroscopy and density functional theory calculations. This study suggested a π -orientation of the oxo group relative to the native C–H bond (in this orientation, the oxo is oriented away from the substrate cavity as shown in Scheme 1, bottom right).⁶ The π -orientation was proposed to be an important prerequisite

Scheme 1. Proposed Catalytic Cycle of SyrB2



for chlorination. More recently, this π -orientation of the Fe–oxo axis relative to the substrate was also implied in a related NHFe halogenase, WelO5.⁷ Low-temperature magnetic circular dichroism

Received: November 21, 2016

Published: January 18, 2017

spectroscopy in combination with quantum chemical calculations were used to define the electronic structure properties associated with geometric structure of the $(\text{SyrB2})\text{Fe}^{\text{IV}}=\text{O}$ intermediate.⁸ The study revealed a π -anisotropy of the $\text{Fe}^{\text{IV}}=\text{O}$ bond with the enhanced π -reactivity in the direction of the substrate cavity. Besides chlorination, SyrB2 was also demonstrated to catalyze hydroxylation depending on the substrate⁹ or azidation/nitration if the non-native (N_3^- or NO_2^-) anions were present in SyrB2 (instead of Cl^-).¹⁰ The substrate-dependent selectivity was attributed to a substrate positioning with respect to the Fe center.^{9,11} This was investigated by HYSCORE spectroscopy applied to the $\{\text{FeNO}\}^7$ complex in SyrB2 with different deuteriated substrates.¹¹ The perpendicular orientation of the NO group relative to the substrate is consistent with the previously defined π -orientation of the oxo group with respect to the substrate C–H bond.⁶

Reactivity and selectivity of the halogenase SyrB2 have also captivated the attention of theoretical groups.^{12–16} These computational studies proposed various reaction mechanisms for chlorination versus hydroxylation: (i) protonation of the $\text{Cl}-\text{Fe}^{\text{III}}-\text{OH}$ intermediate to form $\text{Cl}-\text{Fe}^{\text{III}}-\text{OH}_2$,¹² (ii) concomitant H atom abstraction and radical chlorination;¹³ (iii) propensity for hydroxylation versus halogenation dependent on the delivery of the substrate into the cavity;¹⁴ (iv) coordination isomerism of the $\text{Cl}-\text{Fe}^{\text{IV}}=\text{O}$ intermediate;¹⁵ and (v) coordination isomerism of the $\text{Cl}-\text{Fe}^{\text{IV}}-\text{OH}$ intermediate.¹⁶ However, none of these calculations reflected the experimental data, in particular, the NRVS-determined structure of $(\text{SyrB2})\text{Fe}^{\text{IV}}=\text{O}$,⁶ the X-ray characterization of the related halogenase WelO5,⁷ or substrate-dependent selectivity.⁹

In the present study, we build on our previous combined experimental and theoretical investigations of the geometric and electronic structures of $\text{Fe}^{\text{IV}}=\text{O}$ in SyrB2. The geometrical structural models of the active site of SyrB2 and DFT calculations calibrated to these results are employed to complete the catalytic cycle and provide insight into the key physicochemical factors contributing to chlorination versus hydroxylation selectivity in SyrB2.

2. COMPUTATIONAL DETAILS

2.1. Structural Model of SyrB2. The cluster models of the active site of SyrB2 in the presence of a substrate consist of one Fe center, the Cl^-/OH^- ligands (for the intermediate resulting from H atom abstraction by the $\text{Fe}^{\text{IV}}=\text{O}$), one crystal water molecule, truncated (His_{116} , His_{235} , succinate) ligands, truncated second-shell (Arg_{254} , Thr_{143} , Glu_{102}) residues, and a substrate radical fragment with the thiocarboxylic group (see Figure S1A). The truncated models with the L-threonine/L-norvaline/L-aminobutyric substrates consist of 89/89/86 atoms. Starting $\text{Cl}-\text{Fe}^{\text{III}}-\text{OH}$ structures for the chlorination and hydroxylation reactions were prepared from the O_2 activation and H atom abstraction steps as described in refs 6 and 8 (see also Figure S1B).

2.2. Density Functional Theory Calculations. Unless indicated otherwise, all DFT calculations were performed using the G09 program.¹⁷ The hybrid three-parameter Becke's (B3LYP)¹⁸ functional with the zero-damping empirical correction to dispersion (+D3)¹⁹ was used throughout. All of the geometry optimizations of the cluster models were carried out using the def2-SVP basis set, whereas the single-point energies were recomputed with the def2-TZVP basis set. In single-point calculations, to allow for solvation effects, the polarizable continuum model (PCM) was used with a dielectric constant reflecting the protein environment ($\epsilon_r = 4.0$). In this case, the PCM appears to be a plausible approach as judged from the comparison with QM/MM calculations from ref 16 that provide reaction energies for chlorination versus hydroxylation that are comparable to results from this study. The smaller models used in section 3.3 were optimized in the gas phase at the

B3LYP+D3/def2-TZVP level of theory. Reaction and activation Gibbs free energies were evaluated using vibrational analyses of systems with fixed atoms²⁰ according to the equation:

$$\Delta G^{(\pm)} = \Delta E_{\text{el,solv}}^{(\pm)} + \Delta E_{\text{ZPE}}^{(\pm)} - RT \Delta \ln q_{\text{vib}}^{(\pm)} q_{\text{rot}}^{(\pm)} q_{\text{trans}}^{(\pm)}$$

where $\Delta E_{\text{el,solv}}^{(\pm)}$ is the reaction (or activation) energy of the solvated system (at the B3LYP+D3/def2-TZVP/PCM_(ε_r=4.0)//B3LYP+D3/def2-SVP level), $\Delta E_{\text{ZPE}}^{(\pm)}$ is the change in zero-point energy, and $-RT \Delta \ln q_{\text{vib}}^{(\pm)} q_{\text{rot}}^{(\pm)} q_{\text{trans}}^{(\pm)}$ accounts for the change in the reaction (or activation) entropic terms and the thermal correction to the enthalpy as obtained from a frequency calculation (at 298 K, 1 atm; ideal-gas approximation) on top of optimized geometries.

Constrained density functional theory (cDFT)²¹ was employed using the NWChem 6.1.1 program.²² The single-point cDFT (and related) calculations were performed at the B3LYP/def2-TZVP/COSMO ($\epsilon = 4.0$) level of theory on top of B3LYP+D3/def2-SVP/PCM ($\epsilon = 4.0$) optimized geometries obtained from the G09 program. For the COSMO in the NWChem program, the atomic radii were set to 1.3 (H), 1.83 (N), 1.72 (O), 2.00 (C), 2.05 (Cl), 2.6 (S), and 2.223 Å (Fe), and the solvent-accessible surface to 0.5 Å.

3. RESULTS AND ANALYSIS

3.1. Chlorination versus Hydroxylation: The Native L-Threonine Substrate. The $\text{Fe}^{\text{IV}}=\text{O}$ intermediate with the oxo group oriented away from the substrate cavity was suggested in ref 6 to cleave the C–H bond of the native substrate via a π -attack (see Introduction). This would lead to an $\text{HO}-\text{Fe}^{\text{III}}-\text{Cl}$ intermediate poised for chlorination due to the shorter distance between the substrate carbon radical and the Cl^- ligand relative to the OH^- ligand (by ~0.5 Å considering ionic radii). Alternatively, with the oxo group oriented toward the substrate cavity, H atom abstraction (HAA) would proceed via a σ -attack to produce an $\text{HO}-\text{Fe}^{\text{III}}-\text{Cl}$ intermediate poised for hydroxylation due to the favorable distance between C^\bullet and OH^- relative to the Cl^- (by ~0.5 Å considering ionic radii).⁶ Indeed, for the σ -trajectory of the C–H bond activation, the Gibbs free energy barriers (ΔG^\ddagger) for the chlorination versus hydroxylation pathways were calculated to be 9.6 versus 3.3 kcal mol⁻¹ (Figure S2). Alternatively, starting from the product of the π pathway of ref 6 (1_{Thr} in Figure 1), chlorination versus hydroxylation from the $\text{HO}-\text{Fe}^{\text{III}}-\text{Cl}$ intermediate have essentially the same ΔG^\ddagger values (5.5 vs 5.7 kcal mol⁻¹ from Figure S2B). However, a small conformational change in the substrate starting from 1_{Thr} gives the structure 2_{Thr} (Figure 1) that is more stable by 2.3 kcal mol⁻¹. 2_{Thr} maintains the π orientation and has a more pronounced asymmetry between the $\text{C}^\bullet--\text{Cl}^-$ and $\text{C}^\bullet--\text{OH}^-$ distances with Cl^- closer to the C^\bullet relative to OH^- by ~1.3 Å (considering ionic radii; see Figure S3A). Starting from 2_{Thr} , chlorination was found to be lower in energy than hydroxylation by $\Delta\Delta G^\ddagger = 1.5$ kcal mol⁻¹ ($\Delta\Delta E^\ddagger/\Delta\Delta H^\ddagger = 0.4/1.4$ kcal mol⁻¹) despite the larger thermodynamic driving force for hydroxylation that is favored by $\Delta\Delta G_0 = 8.4$ kcal mol⁻¹ ($\Delta\Delta E_0/\Delta\Delta H_0 = 12/10$ kcal mol⁻¹, at right in Figure 1). The fact that the product of hydroxylation is ~10 kcal mol⁻¹ more stable than the product of chlorination is attributed to the stronger C–OH bond (cf., the experimental bond dissociation enthalpy of C–OH vs C–Cl in $\text{C}_2\text{H}_5\text{OH}$ vs $\text{C}_2\text{H}_5\text{Cl}$ is 94 vs 84 kcal mol⁻¹).²³ These results are in contrast to the expectation based on the Bell–Evans–Polanyi principle that predicts a lower barrier for a more exergonic (exothermic) reaction.

To evaluate the “net” effect of non-thermodynamic contributions to the barriers of chlorination and hydroxylation from 2_{Thr} , Marcus theory²⁴ was employed (Figure 2). Using this theory, the calculated activation energy ΔE^\ddagger is a function of the reaction energy and the intrinsic activation energy (ΔE_0 and

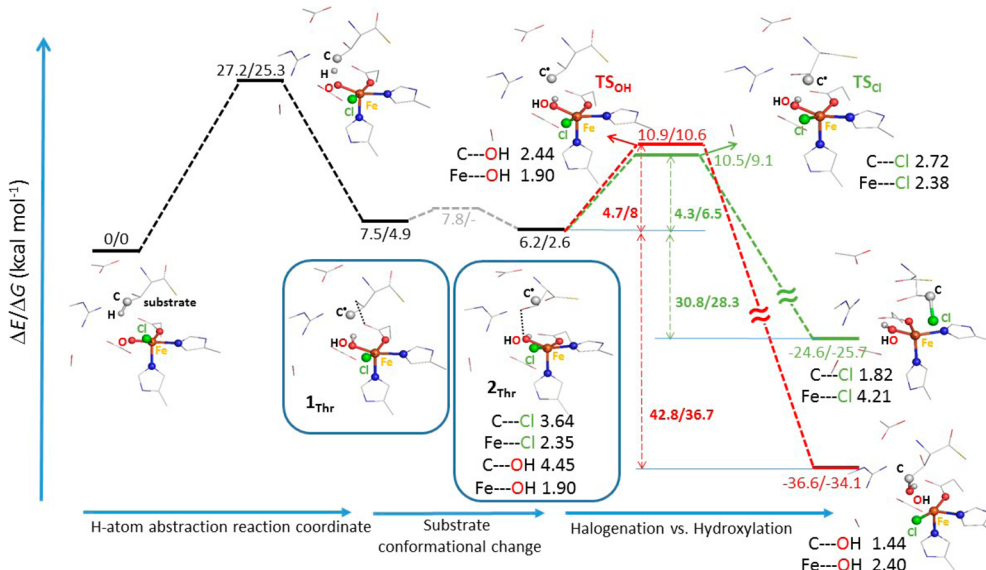


Figure 1. Chlorination versus hydroxylation (in green vs red) from the $\text{Cl}-\text{Fe}^{\text{III}}(S=5/2)-\text{OH}$ product of the H atom abstraction pathway (black), proceeding via the $\text{Cl}-\text{Fe}^{\text{IV}}=\text{O}$ π -attack on the native substrate L-Thr. The relative potential energies and Gibbs free energies are in kcal mol^{-1} , and the key geometric parameters are in angstroms. Note that the water molecule present in the cluster model (from Figure 9A in ref 8) is not depicted. The relative enthalpies are provided in Figure S2. For a detailed comparison of two substrate-radical conformations 1_{Thr} versus 2_{Thr} , see Figure S3A. The dependence of equilibrium geometries on a basis set was tested by performing geometry optimizations for 2_{Thr} and the related transition states for chlorination and hydroxylation, using a combined basis set (def2-TZVP for Fe, ligating atoms, and the terminal C atom of the substrate; def2-SVP for the rest). In comparison with the def2-SVP equilibrium geometries, the geometric changes are small, which translates into small changes of calculated reaction energies (cf., 4.5 and 5.1 kcal mol^{-1} for chlorination and hydroxylation using the hybrid basis set for geometry optimizations vs 4.3 and 4.7 kcal mol^{-1} with the def2-SVP equilibrium geometries).

$\Delta E^{\ddagger}_{\text{int}}$ along the horizontal and vertical axes in Figure 2, respectively), the latter corresponding to the activation energy of a “thermo-neutralized” reaction. Thus, from Figure 2 (and its correlation to the calculations in Figure 1, see caption), “thermo-neutralized” chlorination (starting from 2_{Thr}) is favored over “thermo-neutralized” hydroxylation by $\Delta \Delta E^{\ddagger}_{\text{int}} = 4.6 \text{ kcal mol}^{-1}$ ($\Delta \Delta H^{\ddagger}_{\text{int}}/\Delta \Delta G^{\ddagger}_{\text{int}}$ of $5.2/4.8 \text{ kcal mol}^{-1}$). Alternatively, as can be inferred from the plot in Figure 2 (point “x”), hydroxylation would be favored over chlorination by $\sim 4 \text{ kcal mol}^{-1}$ if chlorination had the same intrinsic barrier as hydroxylation of $20.5 \text{ kcal mol}^{-1}$ (i.e., for $\Delta \Delta E^{\ddagger}_{\text{int}} = 0 \text{ kcal mol}^{-1}$, hydroxylation is favored by its thermodynamic contribution). Importantly, this analysis shows that chlorination, in comparison to hydroxylation, is intrinsically more accessible, which more than compensates for its lower exothermicity. Geometric and electronic factors that contribute in Syrb2 to halogenation over hydroxylation selectivity for the native substrate are analyzed below.

In considering the factors controlling selectivity, the geometric structures of 2_{Thr} (Figure 1) and the transition states of chlorination and hydroxylation (labeled TS_{Cl} and TS_{OH} in Figure 1) are evaluated first. In 2_{Thr} , the Fe^{III} ion is centered in the square pyramidal (SP) ligand field, with both the Cl^- and the OH^- equatorial and *cis* to each other (the z -axis is the open position of the five-coordinate SP Fe^{III} center). The $\text{Fe}-\text{Cl}$ and $\text{Fe}-\text{OH}$ vectors are thus mutually perpendicular. As for the substrate location, the C radical is closer to Cl^- than to OH^- (as indicated earlier), above the $\text{Fe}-\text{Cl}$ bond vector, perpendicular to the $\text{Cl}-\text{Fe}-\text{OH}$ plane, and *trans* to the axial histidine ligand. In going from 2_{Thr} to TS_{Cl} , there is no significant change in the SP arrangement around the Fe^{III} center. Notably the $\text{Fe}-\text{Cl}$ bond elongates by only 0.03 Å (from 2.35 to 2.38 Å), while the C^{\bullet} shifts from 3.64 to 2.72 Å with respect to the Cl^- , remaining

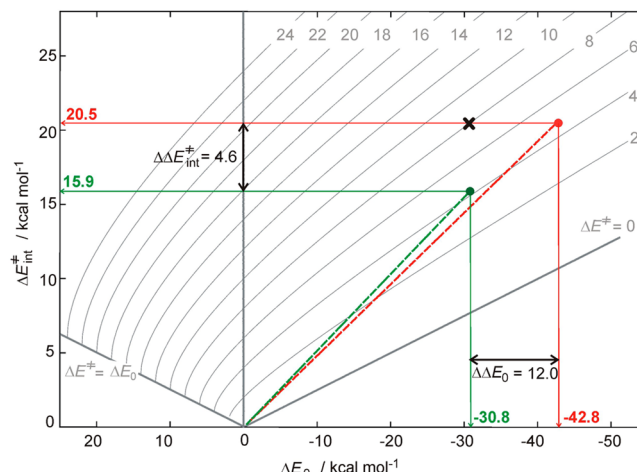


Figure 2. Isocontour plots of the activation energy (ΔE^{\ddagger}), which is, according to Marcus theory,²⁴ dependent on two variables: the reaction energy (ΔE_0 along the horizontal axis) and the intrinsic activation energy ($\Delta E^{\ddagger}_{\text{int}}$ along the vertical axis) [$\Delta E^{\ddagger} = \Delta E^{\ddagger}_{\text{int}} + \Delta E_0/2 + \Delta E_0^2/(16 \times \Delta E^{\ddagger}_{\text{int}})$; for more details on the Marcus theory analysis, see Figure S4A]. From the computational results for the native substrate L-Thr, from Figure 1, the green and red circles positioned at $(\Delta E_0, \Delta E^{\ddagger}) = (-30.8, 4.3)$ and $(-42.8, 4.7)$ in the plot define the intrinsic activation energies of chlorination and hydroxylation of 15.9 and 20.5 kcal mol^{-1} , respectively. The point “x” with $(\Delta E_0, \Delta E^{\ddagger}_{\text{int}}) = (-30.8, 20.5)$ is associated with the activation barrier of 8 kcal mol^{-1} , and relates to chlorination if it had the same intrinsic barrier as hydroxylation. The analogous Gibbs free-energy plot is given in Figure S4B.

perpendicular to the $\text{Cl}-\text{Fe}-\text{OH}$ plane. Similarly, the Fe^{III} in TS_{OH} maintains its SP ligand field with no change in the $\text{Fe}-\text{OH}$ bond length relative to 2_{Thr} (1.90 Å), but the C^{\bullet} shifts from

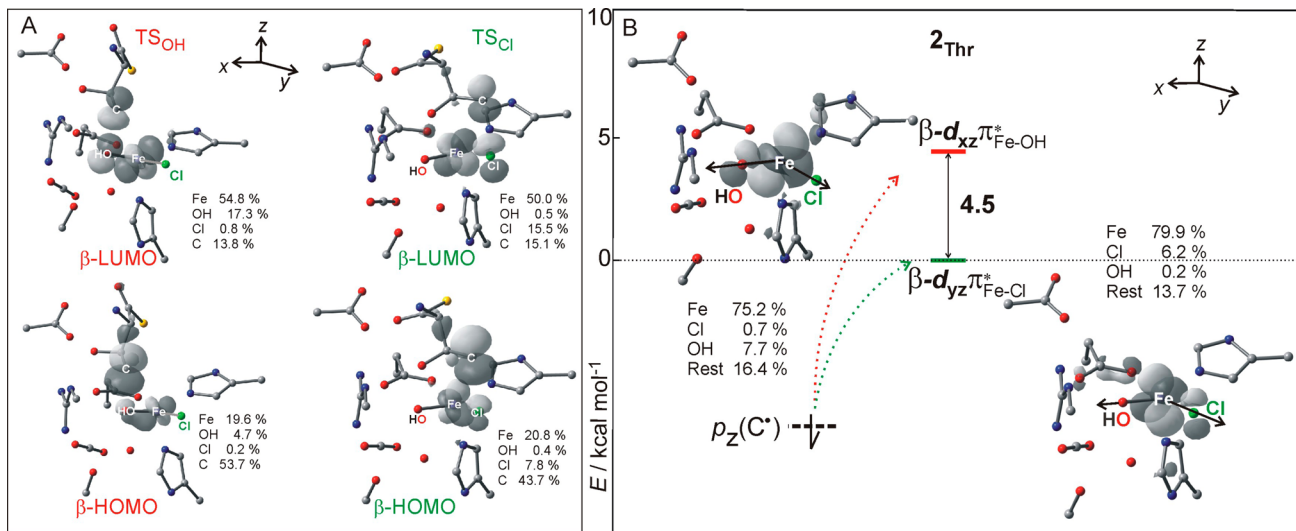


Figure 3. (A) Frontier molecular orbitals, β -HOMO and β -LUMO, and their atomic composition at the TS_{Cl} and TS_{OH} structures from Figure 1. (B) The nature and relative energies of two frontier molecular orbitals calculated for the substrate-radical intermediate $\mathbf{2}_{\text{Thr}}$ (in the absence of the substrate). The lower- and higher-energy FMOs, $d\pi_{\text{Fe-Cl}}^*$ and $d\pi_{\text{Fe-OH}}^*$, are operative in chlorination and hydroxylation, respectively. The arrows indicate the interaction of the substrate orbital with FMOs, while in section 3.4 these are linked more specifically to electron transfer from the substrate to the Fe center.

Table 1. Gibbs Free Energy Barriers for Chlorination and Hydroxylation of Different Substrate Radicals That Result from the H-Atom Abstraction (HAA) Trajectory^a

OH-Fe ^{III} -Cl intermediate ^b	HAA trajectory	chlorination ΔG^\ddagger	hydroxylation ΔG^\ddagger	selectivity ⁱ $\Delta\Delta G^\ddagger$	experimental product analysis: ^j OH vs Cl product (%)
σ-Thr ^c	σ	9.6	3.3	-6.3	13:87
σ-NvaCS ^d	σ	3.1	0.8	-2.3	95:5 ^k
σ-NvaC4 ^d	σ	6.7	6.3	-0.4	35 ^l :65
σ-Aba ^e	σ	10.8	7.0	-3.8	69:31
1 _{Thr} ^f	π	5.5	5.7	+0.2	13:87
2 _{Thr} ^f	π	6.5	8.0	+1.5	13:87
NvaCS ^g	π	5.5	5.0	-0.5	95:5 ^k
NvaC4 ^g	π	5.9	7.0	+1.1	35 ^l :65
Aba ^h	π	5.4	5.3	-0.1	69:31

^aFor comparison, the experimental data from ref 9 are provided in the last column. All energies are in kcal mol⁻¹. ^bH atom abstraction and hydroxylation/chlorination pathways with different substrates along with all relevant structures and their relative energies and geometric parameters are depicted in Figure S2. ^cThe C[•]/ferric intermediate results from σ-HAA activation of L-threonine by Fe^{IV}=O, with the oxo oriented toward the substrate cavity. ^dThe C[•]/ferric intermediate results from σ-HAA activation at the C₅ or C₄ site of L-norvaline by Fe^{IV}=O, with the oxo oriented toward the substrate cavity. ^eThe C[•]/ferric intermediate results from σ-HAA activation of L-aminobutyric acid by Fe^{IV}=O, with the oxo oriented toward the substrate cavity. ^fThe 1_{Thr} and 2_{Thr} intermediates described in section 3.1. ^gThe C[•]/ferric intermediate results from π-HAA activation at the C₅ or C₄ site of L-norvaline by Fe^{IV}=O, with the oxo oriented away from the substrate cavity. ^hThe C[•]/ferric intermediate results from π-HAA activation at the terminal methyl group of L-aminobutyric acid by Fe^{IV}=O, with oxo oriented away from the substrate cavity. ⁱChlorination (hydroxylation) is favored if $\Delta\Delta G^\ddagger > 0 (< 0)$. ^jTaken from ref 9. ^kThe substrate was deuterated at the C₄ site; 5% of the product is chlorinated at C₄. ^lThe substrate was deuterated at the C₅ site; 13% and 22% of the product is hydroxylated at C₄ and C₅, respectively.

4.45 to 2.44 Å from the OH⁻ so that the C[•]--OH vector becomes perpendicular to the Cl-Fe-OH plane with C[•] located above OH⁻ (see Figure 1, and expanded structures are given in Figure S3B).

With respect to electronic structure contributions to the intrinsic barriers, the key FMOs are given in Figure 3. Given the C[•] position with respect to the Cl⁻ or OH⁻ ligand at TS_{Cl} or TS_{OH} (described above), the respective β-HOMOs are identified as the $\beta\text{-p}(C^\bullet)$ orbital with admixture of $\beta\text{-d}\pi^*$ along either the Fe-Cl or the Fe-OH bond (Figure 3A), while the respective β-LUMOs have the $\beta\text{-d}\pi_{\text{Fe-Cl}}^*$ or $\beta\text{-d}\pi_{\text{Fe-OH}}^*$ character mixed with the $\beta\text{-p}(C^\bullet)$ (Figure 3A). From Figure 3, there are two different orthogonal, electron-accepting Fe-d π^* orbitals, one along the Fe-Cl axis and one along the Fe-OH axis, both perpendicular to the Cl-Fe-OH plane. These are suggested to

play key roles in the chlorination versus hydroxylation selectivity of SyrB2. Indeed, as shown in Figure 3B, the energies of these $\beta\text{-d}\pi_{\text{Fe-Cl}}^*$ and $\beta\text{-d}\pi_{\text{Fe-OH}}^*$ orbitals at $\mathbf{2}_{\text{Thr}}$ (in the absence of the substrate C[•]) differ by 4.5 kcal mol⁻¹, with d $\pi_{\text{Fe-Cl}}^*$ lying lower in energy. This energy difference between the two FMOs is similar to the difference between the intrinsic activation energies of chlorination and hydroxylation (i.e., 4.6 kcal mol⁻¹ in favor of chlorination, Figure 2). It is this energy difference between two crucial FMOs that makes chlorination kinetically competitive with hydroxylation; the hydroxylation would otherwise have an activation barrier lower by ~4 kcal mol⁻¹ due to the larger exothermicity of the hydroxylated product. Up to this point, the intrinsic selectivity versus the energy splitting between two FMOs is an empirical correlation that is further evaluated in section 3.3 and is related to the mechanism of

chlorination/hydroxylation that is analyzed in section 3.4. Effects that destabilize Fe-d π^* along the Fe-OH bond relative to the Fe-d π^* along the Fe-Cl bond in SyrB2 are analyzed in section 3.3.

3.2. Orientation Dependence of Chlorination versus Hydroxylation. From ref 6, the σ -pathway for H atom abstraction by (SyrB2)Fe^{IV}=O, with the oxo oriented toward the substrate L-Thr, was proposed to result in substrate hydroxylation because of the favorable C \bullet --OH distance. This prediction was confirmed in section 3.1 (from Table 1, hydroxylation is favored by $\Delta\Delta G^\ddagger$ of -6.3 kcal mol $^{-1}$ for σ -Thr). In agreement with this, when the non-native substrate L-norvaline (Nva) was evaluated with a σ orientation for HAA (oxo toward the substrate cavity), both the terminal C₅ and the adjacent C₄ sites in Nva were found to result in a lower Gibbs free-energy barrier for hydroxylation relative to chlorination by $\Delta\Delta G^\ddagger = -2.3$ kcal mol $^{-1}$ at C₅ and by -0.4 kcal mol $^{-1}$ at C₄ (σ -NvaC5/C4 in Table 1). These findings clearly demonstrate that the σ -trajectory for HAA performed by the oxo that is oriented toward the substrate leads to the C \bullet /HO-Fe^{III}-Cl intermediate, from which hydroxylation is favored. In contrast, from section 3.1, the π -trajectory for the native L-Thr leads to an intermediate with the OH $^-$ oriented away from the substrate radical, favoring chlorination (2_{Thr} in Table 1). Here, we have also evaluated the π -orientation for the C₅ and C₄ sites of Nva. For this orientation, while chlorination does mostly occur on the C₄ site ($\Delta G^\ddagger = 7.0$ vs 5.9 kcal mol $^{-1}$ for hydroxylation vs chlorination; NvaC4 in Table 1), Nva is in fact found to be preferably hydroxylated at C₅ ($\Delta G^\ddagger = 5.0$ vs 5.5 kcal mol $^{-1}$ for hydroxylation vs chlorination; NvaC5 in Table 1). The energetics of the hydroxylation/chlorination pathways associated with the π -channel for HAA from Nva are in fact in better agreement with the experimental data than those associated with the σ -channel: experimentally, the C₅ site is more hydroxylated (95% of the hydroxylated product),⁹ while the C₄ site is more chlorinated (65%).⁹ Another non-native substrate, L-amino-butyric acid that is experimentally known to be hydroxylated/chlorinated in a ratio of 69:31%,⁹ was also calculated. The π -trajectory has essentially equivalent barriers for hydroxylation and chlorination, while the σ -channel leads to hydroxylation (Aba vs σ -Aba in Table 1). Thus, the π -channel for HAA, which is a required prerequisite for the less thermodynamically favorable chlorination (as analyzed in section 3.1), can also allow hydroxylation. Importantly, such a change in selectivity with the π -orientation does not reflect either a difference in the thermodynamics of hydroxylation versus chlorination ($\Delta\Delta G_0$), as these are approximately the same for all of the systems studied (see Figure S2), or a difference in ligand field, as this remains the same over the series (all having five-coordinate square-pyramidal Fe^{III}-hydroxy centers).

An effect that tunes the reaction selectivity in these π -oriented systems enabling either chlorination or hydroxylation is the orientation of the substrate C \bullet with respect to the Cl-Fe-OH plane. Its orientation, defined by the dihedral angle α between the plane containing C \bullet --Cl vector and the Cl-Fe-OH plane, varies for the different C \bullet /HO-Fe^{III}-Cl π -oriented intermediates from 72° (2_{Thr}) through 69° (NvaC4), 56° (Aba), and 51° (1_{Thr}) to 41° (NvaC5). For chlorination (from the calculations given in Figure S2), the C \bullet at TS_{Cl} maintains roughly the same orientation as in the associated intermediate ($\alpha = 79^\circ, 62^\circ, 51^\circ, 50^\circ$, and 44°). Alternatively, for hydroxylation, α is very similar in all of the TS_{OH} structures (falling in the range between 42° and 36°). Thus, the orientation dependence of $\Delta\Delta G^\ddagger$ is correlated

with the angle α (essentially the same in the reactant and the TS_{Cl}) and reflects the amount the intermediate has to distort to reach the TS_{OH} structure (the larger is the distortion, the more positive is $\Delta\Delta G^\ddagger$). From the $\Delta\Delta G^\ddagger$ versus α plot in Figure 4A,

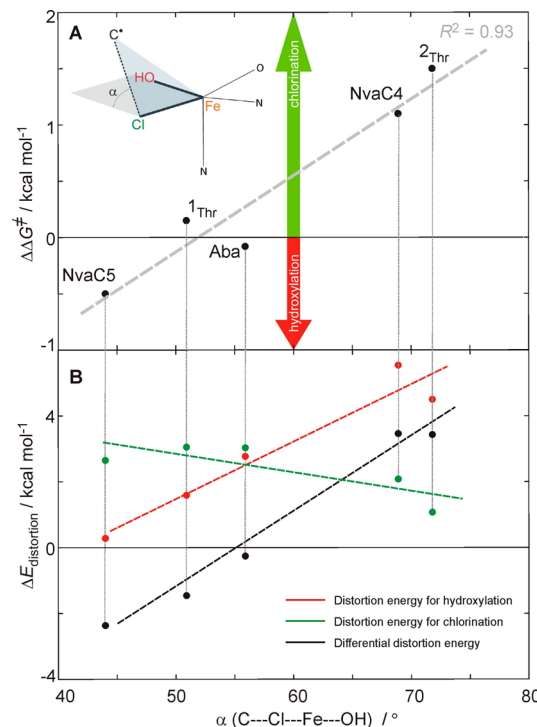


Figure 4. (A) Orientation dependence of chlorination versus hydroxylation selectivity in SyrB2 for the series of substrates studied experimentally in ref 9: the C₅ and C₄ sites of L-norvaline (NvaC5 and NvaC4), L-aminobutyric acid (Aba), and L-threonine with two different conformations (1_{Thr} and 2_{Thr} from Figures 1 and S3A), all activated through the π -channel for HAA. The positive value of $\Delta\Delta G^\ddagger$ ($= \Delta G^\ddagger_{\text{hydroxylation}} - \Delta G^\ddagger_{\text{chlorination}}$) reflects a lower barrier for chlorination, while hydroxylation is favored if $\Delta\Delta G^\ddagger < 0$. The $\Delta\Delta G^\ddagger$ is plotted against the dihedral angle α (= C \bullet --Cl--Fe---OH) at Cl-Fe^{III}--OH intermediate geometries (α depicted in the inset). For each of the substrates, the TS_{Cl} and TS_{OH} structures are shown in Figure S2. (B) The distortion energy ($\Delta E_{\text{distortion}}$), defined as the energy required for distorting a substrate and the active site of SyrB2 to reach the transition state geometry of hydroxylation and chlorination along with the associated differential distortion energy ($\Delta E_{\text{distortion}} = \Delta E_{\text{distortion[hydroxylation]}} - \Delta E_{\text{distortion[chlorination]}}$) as calculated for different substrates. Note that $\Delta E_{\text{distortion}}$ for hydroxylation starting from the substrate and the SyrB2 site of 2_{Thr} is corrected by +3 kcal mol $^{-1}$, which is due to the change in a number of H-bonds in going from 2_{Thr} to TS_{OH}. The energy cycle associated with the evaluation of distortion energies is shown in Figure S5.

chlorination (green arrow) exhibits the largest preference for the most perpendicular orientation of the C \bullet --Cl vector relative to the Cl-Fe-OH plane (72° at 2_{Thr}), whereas hydroxylation is mostly preferred in the NvaC5 system, which has the most parallel orientation of C \bullet --Cl vector to the Cl-Fe-OH plane at the intermediate (44°). For the Aba system that has an intermediate orientation between those in NvaC5 and 2_{Thr} (56° in Figure 4A), chlorination and hydroxylation have comparable ΔG^\ddagger values. The fact that these correlations reflect the amount of reactant \rightarrow TS_{OH} distortion is further supported by the analyses in Figure 4B. This gives the distortion energy ($\Delta E_{\text{distortion}}$) for hydroxylation (red) and chlorination (green), which is defined as

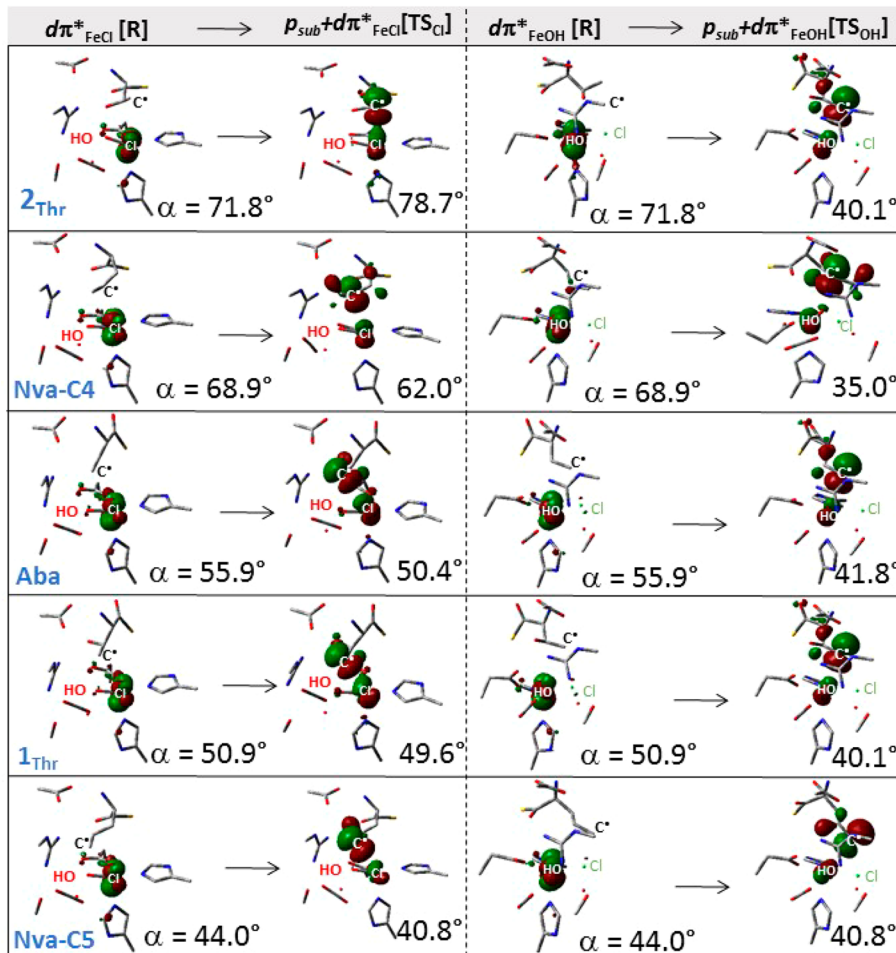


Figure 5. Two $d\pi^*_{\text{FeCl}}$ and $d\pi^*_{\text{FeOH}}$ FMOs at the $\text{Cl}-\text{Fe}^{\text{III}}-\text{OH}$ intermediate geometries (the first and third columns, respectively), as calculated for different substrates (rows) and their overlap with the substrate p orbital (β -HOMO) at the respective TS_{Cl} and TS_{OH} (the second and fourth columns). For chlorination and hydroxylation, structures are displayed with the $\text{Fe}-\text{Cl}$ and $\text{Fe}-\text{OH}$ bond axes pointing out of the plane of the paper, respectively. The magnitude of dihedral angle α (defined in Figure 4) is indicated for all structures.

the energy required for distorting a substrate and the active site of SyrB2 to reach the transition state geometry, plotted against the angle α . For hydroxylation, the $\Delta E_{\text{distortion}}$ increases with α , while for chlorination it remains approximately the same (the green line). Thus, the differential distortion energy $\Delta\Delta E_{\text{distortion}}$ (black line in Figure 4B) exhibits a slope similar to that of $\Delta E_{\text{distortion}}$ for hydroxylation (red line in Figure 4B), with $\Delta\Delta E_{\text{distortion}}$ having a trend similar to that of $\Delta\Delta G^\ddagger$, that is, both favoring hydroxylation in the NvaC5 system and chlorination in 2_{Thr} and NvaC4.

The difference in distortion energy required for reaching TS_{OH} versus TS_{Cl} is linked to a difference in how much the $d\pi^*_{\text{FeCl}}$ versus $d\pi^*_{\text{FeOH}}$ FMO distorts away from its perpendicular orientation relative to the $\text{HO}-\text{Fe}-\text{Cl}$ plane upon the overlap with the substrate radical. In Figure 5, the two FMOs, $d\pi^*_{\text{FeCl}}$ and $d\pi^*_{\text{FeOH}}$ (the first and third columns), are displayed at the $\text{Cl}-\text{Fe}^{\text{III}}-\text{OH}$ intermediate geometries in the presence of different substrates (each row for one substrate). Following the chlorination pathway (going from the first to second column), the $d\pi^*_{\text{FeCl}}$ π -overlaps with the substrate p orbital (the β -HOMO in the second column). From the comparison of all of the β -HOMOs in the second column of Figure 5, the deviation of the p orbital from its perpendicular orientation relative to the $\text{HO}-\text{Fe}-\text{Cl}$ plane increases with the decrease in the angle α . Consequently, the orientation of $d\pi^*_{\text{FeCl}}$ follows the rotation of

the C^\bullet along the $\text{Fe}-\text{Cl}$ bond to maximize its overlap with the $p(\text{C}^\bullet)$ orbital. This adaptability in the orientation of $d\pi^*_{\text{FeCl}}$ is attributed to the $p(\text{C}^\bullet)$ -mediated orbital mixing between $d\pi^*_{yz}$ (from Figure 3) and the higher-energy $d\pi^*_{xy}$ (axes defined in Figure 3B) that increases with the decrease in α (Table S2). For hydroxylation, where the $d\pi^*_{\text{FeOH}}$ π -overlaps with the substrate p orbital at TS_{OH} , the $d\pi^*_{\text{FeOH}}$ is also rotated to achieve good overlap with the substrate $p(\text{C}^\bullet)$ orbital (from the third to fourth column in Figure 5). However, the $d\pi^*_{\text{FeOH}}$ rotation is limited and approximately the same for all systems (see the β -HOMOs in the fourth column of Figure 5). This is rationalized by the limited flexibility in the OH ligand vector orientation, which is anchored by an H-bond to the neighboring monodentate carboxylate group and one from the nearby (crystallographic) water molecule (Table S3). This results in a similar angle α for all calculated TS_{OH} 's, and the change in selectivity is therefore mostly given by how much the intermediate has to distort to reach TS_{OH} .

3.3. Ligand Field Effects on FMOs and Their Contributions to Selectivity. The difference between intrinsic activation barriers of chlorination and hydroxylation (starting from 2_{Thr} in Figure 1) was linked in section 3.1 to the energy difference between two FMOs: $d\pi^*_{\text{Fe-OH}}$ and $d\pi^*_{\text{Fe-Cl}}$. In this section, this correlation is elaborated using small structural

models to elucidate how ligand-field effects on the two FMOs correlate with intrinsic reactivity.

The trend in the intrinsic barrier favoring chlorination with the energy splitting of the $d\pi^*_{Fe-Cl}/d\pi^*_{Fe-OH}$ FMOs was developed using a series of structures with two *cis*-positioned ligands, Cl^- and $X = F^-, OH^-, Cl^-, Br^-,$ and I^- (structures **1-X** in Figure 6).

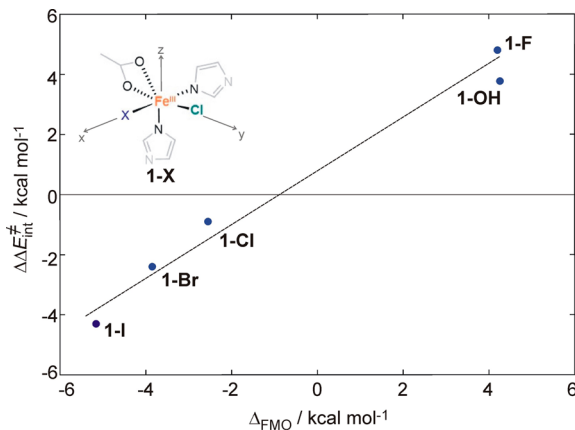


Figure 6. Difference between chlorination and hydroxylation intrinsic activation energies $\Delta\Delta E^\ddagger_{int}$ ($=\Delta E^\ddagger_{int}[\text{halogenation}] - \Delta E^\ddagger_{int}[\text{chlorination}]$) correlated with the FMO energy splitting Δ_{FMO} ($=E[d\pi^*_{xz,Fe-X}] - E[d\pi^*_{yz,Fe-Cl}]$), using five complexes with two *cis*-positioned ligands Cl^- and $X = F^-, OH^-, Cl^-, Br^-,$ and I^- (structure defined in the inset). For clarity, H atoms in all of the structures are not visualized. Reaction pathways were calculated as in Figure S6.

For these structures, the intrinsic barriers for chlorination versus halogenation (fluorination to iodination) were calculated as described in Figure S6 with a methyl radical positioned perpendicular to the transferring atom and correlated with the energy splitting of the $d\pi^*_{Fe-Cl}/d\pi^*_{Fe-X}$ FMOs. This correlation is given in Figure 6. For I, the $\beta-d\pi^*_{Fe-I}$ orbital is ~ 5 kcal mol $^{-1}$ lower in energy than $\beta-d\pi^*_{Fe-Cl}$ (at 0 kcal mol $^{-1}$ on the abscissa), which directly correlates with the low intrinsic barrier for iodination

versus chlorination, favoring iodination by ~ 4 kcal mol $^{-1}$. In contrast, the $\beta-d\pi^*_{Fe-F}$ orbital in **1-F** is ~ 4 kcal mol $^{-1}$ higher in energy than $\beta-d\pi^*_{Fe-Cl}$ and has the highest intrinsic barrier (for fluorination) as compared to chlorination by ~ 5 kcal mol $^{-1}$.

Thus, the Δ_{FMO} ($=E[d\pi^*_{xz,Fe-X}] - E[d\pi^*_{yz,Fe-Cl}]$) correlates with intrinsic reactivity, and we can now consider the ligand field (LF) factors that influence Δ_{FMO} for a series of $Fe^{III}Cl/X$ ($=OH, F, Cl, Br, I$) complexes. First, LF geometries were varied as shown in Figure S7, where calculations of the FMO energy splitting for octahedral (O) versus square-pyramidal (SP) versus trigonal-bipyramidal (TBP) structures show that there is no significant dependence on the structure ($\Delta_{FMO} = 4.2, 3.1, 4.1$ kcal mol $^{-1}$ for O vs SP vs TBP). Next, for a group of five-coordinate square-pyramidal structures $[(NH_3)_3(X)Fe^{III}Cl]$ with $X = OH^-, F^-, Cl^-, Br^-,$ and I^- , we systematically varied the pair of Cl^-/X^- *cis*-equatorial ligands as given in Figure 7. Within this series, the FMO energy splitting varies in a manner similar to that in Figure 6. This allows evaluation of the relative contributions of π donation and ligand electrostatics for $X^- = OH^-, F^-, Cl^-, Br^-,$ and I^- to the energy splitting of these FMOs. Note that the trend in the FMO splitting cannot be simply correlated with the trend observed in the spectrochemical series as this reflects both the π and the σ donation ability of the ligand X rather than differences in π donation. The ability of the ligand X^- to impact the energy of the FMO by π -donation can be quantified by the “destabilization energy” ($E_{\pi,Fe-X}$) that is estimated as the product of c_X^2 (the weighted admixture of ligand p_X character in the $d\pi^*_{Fe-X}$ orbital) and Δ (the energy gap between the “noninteracting” ligand p_X and d_{Fe} orbitals). While Δ can be evaluated directly and gives equivalent results (see Table S1), we employ here an approach (see Supporting Information) that estimates the π -donation contribution to a destabilization energy of a $d\pi^*_{Fe-X}$ relative to the contribution of Cl π -donation to the $d\pi^*_{Fe-Cl}$ energy:

$$E_{\pi,Fe-X} - E_{\pi,Fe-Cl} \cong c_X^2(I_X - I_{Cl}) + E_{\pi,Fe-Cl}\left(\frac{c_X^2}{c_{Cl}^2} - 1\right) \quad (1)$$

Structure	$d\pi^*_{FeCl}$	$d\pi^*_{FeBr}$	$d\pi^*_{FeI}$	$d\pi^*_{FeF}$	$d\pi^*_{FeOH}$
Δ_{FMO} / kcal mol $^{-1}$	-7.6	-2.9	0.3	7.0	5.6
$d\pi^*_{FeI}$					
$\pi\text{-donation of } X:$					
$c^2 \cdot 100 / \%$	28.4	19.1	8.1	6.4	11.5
$I_{\text{expt}} (I_{\text{calcd}}) / \text{kcal mol}^{-1}$	70.5 (74.1)	77.4 (77.3)	83.4 (76.5)	78.4 (66.6)	41.5 (26.9)
$\Delta E_\pi (\Delta E'_\pi) / \text{kcal mol}^{-1}$	> 0	> 0	0	< 0	< 0
Mulliken charge q on $X/Cl:$	-0.08/-0.27	-0.20/-0.26	-0.25/-0.25	-0.44/-0.25	-0.29/-0.26
q'/q^{Cl} :	0.30	0.77	1.00	1.76	1.12

Figure 7. Series of five structures along with their geometric parameters, and the associated energy splittings between two FMOs: $d\pi^*_{Fe-X}$ ($X = I, Br, Cl,$ and OH ; atom label in blue) versus $d\pi^*_{Fe-Cl}$ (the Cl label in green). Weights of the ligand character in the $d\pi^*_{Fe-X}$ (c_X^2), experimental and calculated ionization potentials of X (I_{expt} and I_{calcd}), relative π -donation contributions to $d\pi^*_{Fe-X}$ as calculated using eq 1 by employing I_{expt} or I_{calcd} (ΔE_π or $\Delta E'_\pi$ where $\Delta E_\pi = E_{\pi,Fe-X} - E_{\pi,Fe-Cl}$), and partial Mulliken charges are also provided. The experimental ionization potentials are taken from ref 23. For the dependence of ΔE_π or $\Delta E'_\pi$ on $E_{\pi,Fe-Cl}$ see Figure S8. All of the structures were optimized with a geometric constraint to maintain the square-pyramidal ligand field (X, Cl, and two N atoms were kept in one plane).

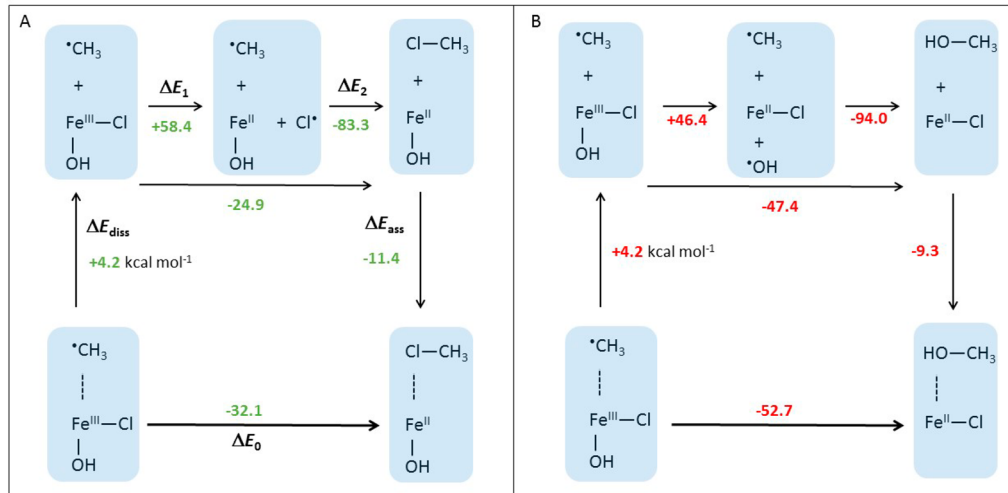


Figure 8. (A) The gas-phase thermodynamic cycle for chlorination of the $\text{CH}_3\cdot$ substrate by complex **1-OH** (depicted in Figure 6), where the reaction energy ΔE_0 is divided into the energy of dissociation of $\text{CH}_3\cdot$ from **1** (ΔE_{diss}), homolytic cleavage of the $\text{Fe}^{\text{III}}-\text{Cl}$ bond in **1** (ΔE_1), the formation of the $\text{H}_3\text{C}-\text{Cl}$ bond (ΔE_2), and the energy of the association of $\text{H}_3\text{C}-\text{Cl}$ with the Fe^{II} complex (ΔE_{ass}). (B) The gas-phase thermodynamic cycle for hydroxylation of the $\text{CH}_3\cdot$ substrate by complex **1**, analogous to the cycle from panel A. The associated enthalpies and Gibbs free energies are provided in Figure S9.

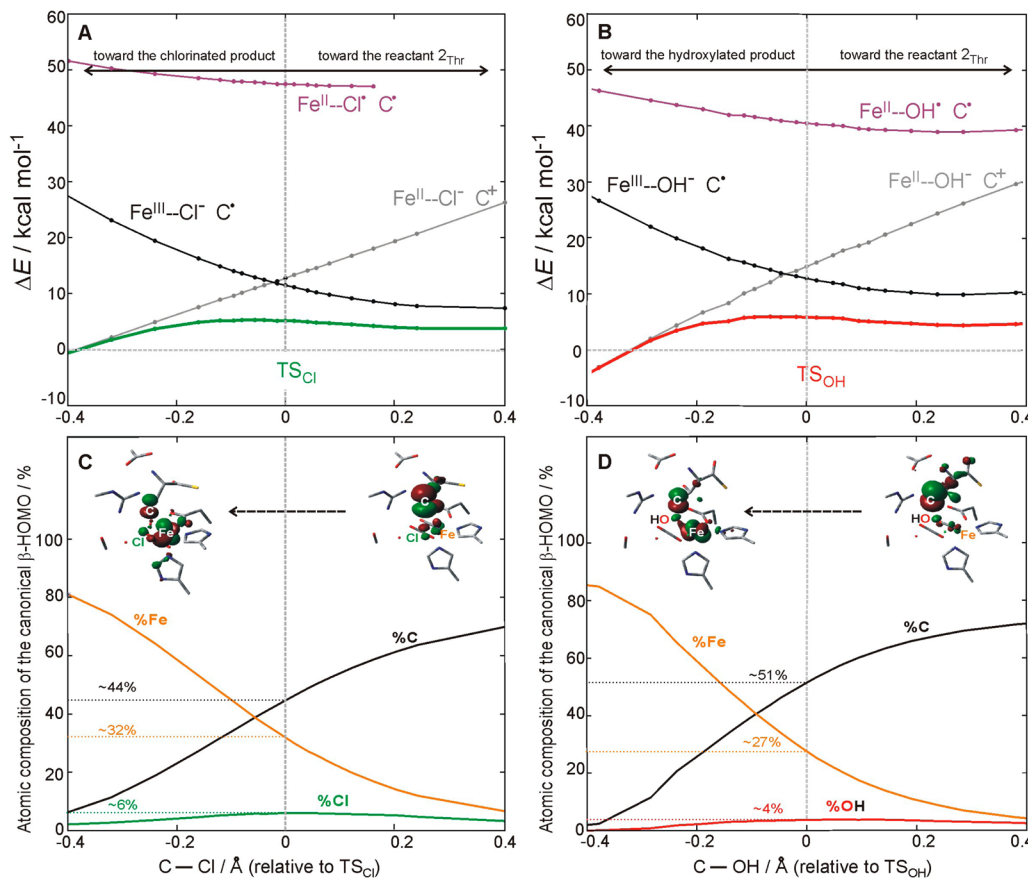


Figure 9. (A) Adiabatic $S = 2$ PES of chlorination (green) from 2_{Thr} and diabatic $S = 2$ PESs of three spin-density constrained states (black, gray, and magenta), all calculated along the TS_{Cl} reaction coordinate (represented by the change in the $\text{C}-\text{Cl}$ bond length relative to TS_{Cl} in going from right to left). (B) Adiabatic $S = 2$ PES of hydroxylation (red) and diabatic $S = 2$ PESs of three spin-density constrained states (black, gray, and magenta), all calculated along the TS_{OH} reaction coordinate (represented by the change in the $\text{C}-\text{OH}$ bond length relative to TS_{Cl} in going from right to left). (C) Evolution of the atomic composition of the β -HOMO along the chlorination reaction coordinate (the same coordinate as in (A)), including the contours of the β -HOMO before (right) and after (left) electron transfer from the substrate to the Fe center. (D) Evolution of the atomic composition of the β -HOMO along the hydroxylation reaction coordinate (the same coordinate as in (B)), including the contours of the β -HOMO before (right) and after (left) electron transfer from the substrate to the Fe center.

where I_X is the ionization potential of X, c_X^2 is defined above, and $E_{\pi,\text{Fe}-\text{Cl}}$ is the π -donation contribution to the destabilization energy of the $d\pi^*_{\text{Fe}-\text{Cl}}$ that is assumed to be positive for π -donation into a $d\pi^*$ orbital. Importantly, for a positive value of $E_{\pi,\text{Fe}-\text{Cl}}$ ($>\sim 2$ kcal mol $^{-1}$), the $E_{\pi,\text{Fe}-\text{I}}$ and $E_{\pi,\text{Fe}-\text{Br}}$ are always larger than the $E_{\pi,\text{Fe}-\text{Cl}}$, while the opposite is true for the $E_{\pi,\text{Fe}-\text{F}}$ and $E_{\pi,\text{Fe}-\text{OH}}$ (see Figure S8). However, this is not the trend reflected in Δ_{FMO} , where $d\pi^*_{\text{Fe}-\text{I}}$ and $d\pi^*_{\text{Fe}-\text{Br}}$ are lower in energy than $d\pi^*_{\text{Fe}-\text{Cl}}$, while $d\pi^*_{\text{Fe}-\text{OH}}$ and $d\pi^*_{\text{Fe}-\text{F}}$ are higher (Figure 7). Considering the fact that X $^-$ and Cl $^-$ ligands in the complexes in Figure 7 are both *trans* to the σ -donating ligand NH $_3$, we can also exclude a *trans* effect contribution to Δ_{FMO} . The trend in Δ_{FMO} does however correlate with differences in the strength of the ligand field. This can be estimated from the relative partial Mulliken charges of the X $^-$ versus Cl $^-$ ligand, as given by the q^X/q^{Cl} quantity at the bottom row of Figure 7. These reflect the fact that lower electron donation leads to more negative charge on the ligand. From Figure 7, while OH $^-$ is a weaker π -donor than Cl $^-$, it is associated with a stronger LF, which leads to a higher-energy $d\pi^*_{\text{Fe}-\text{OH}}$ as compared to the $d\pi^*_{\text{Fe}-\text{Cl}}$ orbital.

3.4. Possible Mechanisms of Chlorination and Hydroxylation. We first consider a “rebound” mechanism. Within this process, the Fe $^{\text{III}}$ –Cl (Fe $^{\text{III}}$ –OH) bond would undergo homolytic cleavage, producing the Cl $^\bullet$ (OH $^\bullet$) moiety that recombines with the substrate C $^\bullet$. Figure 8 presents thermodynamic cycles for the chlorination and hydroxylation reactions in Figure S6A that include the two sequential steps, homolysis and recombination. From a comparison of the two cycles, homolysis of the Fe $^{\text{III}}$ –Cl bond is 12 kcal mol $^{-1}$ less favorable than homolytic cleavage of the Fe $^{\text{III}}$ –OH bond (cf., ΔE_1 values in Figure 8A and B), which qualitatively parallels the experimental (and calculated) ionization potentials of Cl $^-$ and OH $^-$ (IP[Cl $^-$ \rightarrow Cl $^\bullet$] = 3.6²³ (3.3) eV; IP[OH $^-$ \rightarrow OH $^\bullet$] = 1.8²³ (1.2) eV). Also, the recombination of the radicals (ΔE_2 in Figure 8) is calculated to favor hydroxylation by \sim 11 kcal mol $^{-1}$ (cf., the experimental bond dissociation energy of CH $_3$ –Cl vs CH $_3$ –OH is 83 vs 92 kcal mol $^{-1}$).²³ From these numbers, chlorination would not compete with hydroxylation.

Another possible mechanism would correspond to a process in which the Fe $^{\text{III}}$ –Cl (Fe $^{\text{III}}$ –OH) bond spin polarizes to Fe $^{\text{II}}$ –Cl $^\bullet$ (Fe $^{\text{II}}$ –OH $^\bullet$) upon the attack of the substrate. Figure 9A presents the reaction coordinate for chlorination from 2_{Thr} from right to left that includes the DFT potential energy surface (PES) of the electronic ground state (green curve). The analogous PES for hydroxylation is shown in Figure 9B (red curve). Constrained density functional theory (cDFT) allows localization of the spin density along the reaction coordinate. Thus, cDFT is suitable for the evaluation of the energy required for Fe $^{\text{III}}$ –X \rightarrow Fe $^{\text{II}}$ –X $^\bullet$ spin polarization along the reaction coordinate in Figure 9. Within the cDFT approach, an Fe $^{\text{II}}$ –X $^\bullet$ state can be optimized by constraining one unpaired α electron on X (=Cl or OH), four unpaired α electrons on Fe, and one unpaired β electron on the substrate. This constraint, maintained along the chlorination and hydroxylation reaction coordinates, allows for construction of “diabatic” PESs of the spin-polarized Fe $^{\text{II}}$ –Cl $^\bullet$ and Fe $^{\text{II}}$ –OH $^\bullet$ states (magenta curves in Figure 9A and B). From valence bond theory, a diabatic state preserves its character with a change in a molecular geometry. This differs from an adiabatic state that can be considered as a linear combination of diabatic states with weights that change with molecular geometry. Thus, the adiabatic ground-state PES (reaction barrier in green and red in Figure 9A and B) should result from a strong configuration

mixing of two diabatic (“reactant” and “product”) states that cross each other at the transition state. The “reactant” state is constrained to have the electronic structure of the 2_{Thr} intermediate, that is the HO–Fe $^{\text{III}}$ –Cl/C $^\bullet$ state (the diabatic “reactant” PES is plotted in black in Figure 9A and B). It is evident from Figure 9A and B that the Fe $^{\text{II}}$ –Cl $^\bullet$ /C $^\bullet$ and Fe $^{\text{II}}$ –OH $^\bullet$ /C $^\bullet$ states (in magenta) do not cross with the “reactant” state and are more than 40 kcal mol $^{-1}$ above the associated reaction barriers. Therefore, these states do not appear to participate in chlorination and hydroxylation. This conclusion is further supported by the results from section 3.1, which show no essential change in the Fe–Cl (Fe–OH) bond length in going from the reactant to the transition state, indicating little Fe $^{\text{III}}$ –X \rightarrow Fe $^{\text{II}}$ –X $^\bullet$ polarization occurs upon substrate attack.

Because the Fe $^{\text{II}}$ –X $^\bullet$ state is predicted to be too high in energy to contribute to the chlorination/hydroxylation reactivity, there should be another lower-energy state that mixes with the “reactant” HO–Fe $^{\text{III}}$ –Cl/C $^\bullet$ state at the associated transition state. Indeed, cDFT calculations, imposing four unpaired α electrons on Fe and no unpaired electrons on the substrate and X (=Cl or OH), indicate that such an electron distribution (gray curves in Figure 9A and B) is almost isoenergetic with the “reactant” HO–Fe $^{\text{III}}$ –Cl/C $^\bullet$ electronic structure at the TS_{Cl} (Figure 9A) and TS_{OH} (Figure 9B). The “product” state can be characterized as the HO–Fe $^{\text{II}}$ –Cl/C $^+$ state that differs from the “reactant” state by one β -electron that is mostly transferred from the p orbital of the substrate to the redox-active $d\pi^*_{\text{Fe}-\text{Cl}}$ ($d\pi^*_{\text{Fe}-\text{OH}}$) on the iron center (see FMOs from cDFT calculations in Figure S10). For both chlorination and hydroxylation starting from 2_{Thr}, the diabatic two-state crossing is located \sim 7 kcal mol $^{-1}$ above the top of the barrier of the adiabatic reaction coordinate. Note that the two diabatic PESs are related to the two parabolas used in the Marcus theory analysis in Figures 2 and S4 (this assumes that an electronic coupling between two parabolas is small, i.e., weaker than the couplings of \sim 7 kcal mol $^{-1}$ for chlorination/hydroxylation derived from Figure 9; however, the couplings for the two processes are equivalently large, which justifies the application of the Marcus analysis in Figure 2 for these two adiabatic reactions). These cDFT results indicate that both the chlorination and the hydroxylation reactions are initiated by the electron transfer (ET) from the carbon radical to the Fe $^{\text{III}}$ center, mediated by the Cl $^-$ or OH $^-$ ligand providing a superexchange pathway for ET. This would be followed by the ligand (Cl $^-$ or OH $^-$) transfer to the oxidized substrate.

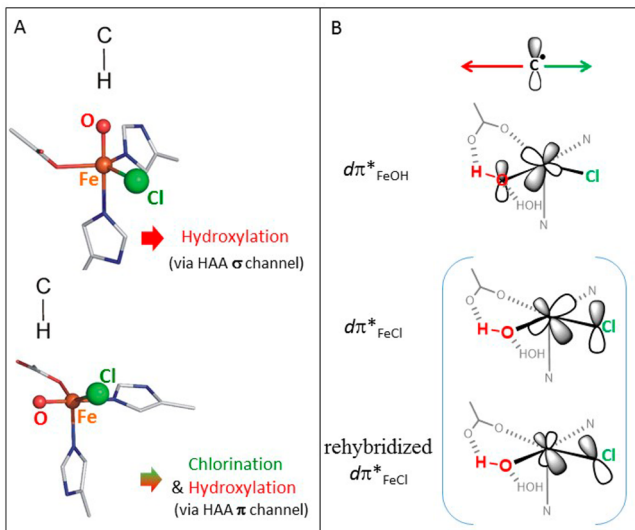
This description of chloride and hydroxide transfer is supported by the evolution of the atomic composition of the β -HOMO from Figure 3A along the reaction coordinate for chlorination and hydroxylation as shown in Figure 9C and D. In both cases, when the substrate carbon approaches the Cl $^-$ or OH $^-$ ligand (going from right to left in Figure 9C and D), the weight of the C and Fe character decreases and increases, respectively, while the Cl or OH contributions to the respective β -HOMOs remain low and essentially constant along the coordinate, as would be expected for a superexchange-enabled ET. At both the TS_{Cl} and the TS_{OH}, the β -HOMO has a significant radical character on the substrate, indicating that both transition states are early in the reaction coordinate. The fact that the superexchange controlled ET is followed by the ligand (Cl $^-$ or OH $^-$) transfer is further supported by the calculated C–Cl (C–OH) bond order at TS_{Cl} (TS_{OH}) that is only \sim 15% (\sim 10%) of the final bond order of the product (see Figure S11). This superexchange mechanism for ET to the Fe is fully in line

with the correlation of selectivity to the energy splitting between the two redox-active FMOs.

4. DISCUSSION

Considering a σ -trajectory for the H atom abstraction reaction (with the oxo oriented toward the substrate cavity), hydroxylation is found to be favored over chlorination for all substrates investigated in this study (section 3.2; see also Scheme 2A).

Scheme 2. (A) The σ -Channel for H-Atom Abstraction from a Substrate by the $\text{Fe}^{\text{IV}}=\text{O}$ Intermediate Leads to Hydroxylation (Top), while the π -Channel Can Lead to Either Chlorination or Hydroxylation (Bottom); and (B) For the π -Channel, the Orientation of the Substrate Enables Either the Cl^- or the OH^- to Rebound Depending on the Relative π -Overlap with the Substrate C Radical^a



^aThe red arrow indicates the region where the π -overlap with OH^- favors hydroxylation, and the analogous arrow in green indicates the region favoring chlorination. Note that the $d\pi^*_{\text{FeCl}}$ FMO can rehybridize to maximize its overlap with the substrate C^\bullet if this radical is not located above the Fe-Cl bond axis.

Thus, this σ -trajectory cannot be operative in SyrB2 in the presence of the native substrate L-Thr that is predominantly chlorinated. Instead, as was already reported in refs 6 and 8, the HAA pathway with the L-Thr is suggested to follow the π -trajectory (with the oxo oriented perpendicular to the substrate cavity). Following the π -trajectory for HAA in SyrB2 with different substrates, the reaction barrier of chlorination is calculated to be comparable (and in some cases favored) to that of the more thermodynamically favored hydroxylation (Scheme 2A). This is associated with a higher intrinsic reactivity toward chlorination due to the lower intrinsic activation barrier (by 4–5 kcal mol⁻¹) as determined by a Marcus theory analysis (section 3.1). Thus, the intrinsic preference for chlorination compensates the thermodynamic propensity for hydroxylation. The difference between intrinsic activation barriers for the “thermo-neutralized” chlorination and hydroxylation reactions correlates to the energy difference between two key frontier molecular orbitals (sections 3.1 and 3.3). One of these FMOs, which results from the antibonding π -interaction along the Fe-Cl bond axis ($d\pi^*_{\text{Fe-Cl}}$), is active in chlorination and is ~4–5 kcal mol⁻¹ lower in energy than the FMO active in hydroxylation, arising from the analogous antibonding interaction along the

Fe-OH bond axis ($d\pi^*_{\text{Fe-OH}}$). These two FMOs are depicted in Figure 3. The FMO energy splitting Δ_{FMO} in the $\text{Cl}-\text{Fe}^{\text{III}}-\text{OH}$ intermediate in SyrB2 is attributed to the differential effect of the ligand field that is larger for OH^- than for Cl^- (section 3.4).

Calculations in this study reveal that the π -orientation can lead to chlorination or hydroxylation depending on the substrate orientation. The native L-threonine substrate and the C₄ site of L-norvaline are predicted to be chlorinated, the C₅ site of L-norvaline hydroxylated, and there is no calculated preference for hydroxylation relative to chlorination for the L-aminobutyric substrate. These results are in agreement with experimental observations of Bollinger and Krebs.⁹ Such a substrate-dependent selectivity derives from the orientation of the C radical with respect to the HO-Fe-Cl plane (Scheme 2B). The analysis from section 3.2 indicates that the orientation effect in SyrB2 is attributed to the distortion that needs to occur for the substrate C radical to achieve good π -overlap with the $d\pi^*_{\text{Fe-OH}}$ FMO at the transition state of hydroxylation. It is this distortion that actually controls selectivity in SyrB2 (as the difference in the intrinsic barrier, related to the FMO energy difference favoring chlorination, is mostly compensated by the differential thermodynamic contribution to the rebound barriers that favors hydroxylation). The distortion to reach the transition state of hydroxylation is related to the fact that the $d\pi^*_{\text{Fe-OH}}$ FMO has a fixed orientation (perpendicular to the Fe-O-H plane) due to the anchoring H-bond of the OH^- group with the coordinated carboxylate group. The analogous π -overlap with the $d\pi^*_{\text{Fe-Cl}}$ FMO does not require such a substrate distortion due to rehybridization of the $d\pi^*_{\text{Fe-Cl}}$ FMO toward the substrate radical. Thus, the orientation effect, which arises from the positioning of the substrate radical above the HO-Fe-Cl plane and the differential FMO orientation flexibility in overlapping with the substrate, corresponds to the differential overlap contribution to chlorination versus hydroxylation selectivity as simplified in Scheme 2B.

The FMO control over selectivity is also consistent with reaction mechanism for chlorination and hydroxylation of the C radical by the HO-Fe^{III}-Cl intermediate. This would be initiated by β -electron transfer from the C^\bullet to the $S = 5/2$ Fe^{III} center through the superexchange mediating Cl^- (OH^-) ligand, which, after the transition state, is followed by the Cl^- (OH^-) transfer (section 3.4). This mechanism is consistent with the correlation of the orbital energy splitting between two key $d\pi^*$ FMOs with differential intrinsic reactivity toward chlorination versus hydroxylation.

Concerning oxidative ligand transfer (rebound) selectivity, it is worth noting that a synthetic high-spin ($S = 2$) nonheme iron model of SyrB2 was demonstrated to halogenate with the unprecedented yield of 30–40%.²⁵ This work along with other studies^{26,27} show that a rebound process in solution is somewhat slow, which allows the escape of a substrate radical from the solvent cage. This leaves an open question on a mechanism for halogenation/hydroxylation by biomimetic nonheme iron complexes in solution. However, radical substrates in solution are less restricted in their diffusive motion than radical substrates in a protein cavity, which would result in specific orientations of the substrate C^\bullet relative to the HO-Fe-Cl plane of a reactive complex. We expect fast rebound to be favored over escape in SyrB2 due to interactions of the substrate radical with the protein cavity cage.

5. CONCLUSIONS

Chlorination versus hydroxylation selectivity was computationally evaluated for different substrates and found to be in a good

agreement with the experimental observations from ref 9. The π -trajectory for H atom abstraction as defined in refs 6 and 8 was calculated to lead to the $S = 2$ five-coordinate HO–Fe^{III}–Cl intermediate with the C[•] substrate, π -oriented relative to both the Cl[−] and the OH[−] ligands. Starting from this ferric intermediate, hydroxylation is thermodynamically favored, but chlorination is intrinsically more reactive. A higher intrinsic chlorination reactivity derives from the energy splitting between two key redox-active d π^* FMOs: the lower is the FMO energy for chlorination relative to that for hydroxylation, the higher is the intrinsic reactivity for chlorination. The orbital splitting arises from the differential ligand-field effect of Cl[−] versus OH[−] on the Fe d π^* orbitals. This factor makes chlorination effectively competitive with hydroxylation. Chlorination versus hydroxylation selectivity is then determined by the orientation of the substrate C[•] with respect to the HO–Fe–Cl plane that is related to the differential overlap of the substrate p orbital with two d π^* FMOs. The differential contribution of the FMOs to chlorination versus hydroxylation selectivity in SyrB2 is related to a reaction mechanism that employs two asynchronous transfers: electron transfer from the substrate radical to the iron center followed by late ligand (Cl[−] or OH[−]) transfer to the substrate.

■ ASSOCIATED CONTENT

Supporting Information

The Supporting Information is available free of charge on the ACS Publications website at DOI: [10.1021/jacs.6b11995](https://doi.org/10.1021/jacs.6b11995).

Figures showing (S1A) structural models of the active site of SyrB2 and (S1B) O₂ activation pathways, (S2) reaction pathways of chlorination/hydroxylation for different substrates, (S3) geometric comparison of two HO–Fe^{III}–Cl structures **1**_{Thr} and **2**_{Thr}, (S4) isocontour plots of the activation Gibbs free energy, (S5) change in chlorination versus hydroxylation selectivity using two different structural models, (S6) energy cycle for a Cl–Fe^{III}–OH intermediate → TS_{Cl/OH} transition, (S7) ligand-field geometries and the associated FMO energy splittings, (S8) estimation of the π -donation contribution to the destabilization energy of the d π^* _{FeX} relative to the contribution of Cl π -donation to the d π^* _{FeX} energy, (S9) thermodynamic cycle for chlorination of the methyl-radical substrate by complex **1**, (S10) cDFT FMOs, and (S11) evolution of three selected Mulliken bond indices along chlorination and hydroxylation reactive mode; Table S1 comparing the ability of the ligand X[−] to impact the energy of the FMO by π -donation; and the derivation of eq 1 from the main text ([PDF](#))

Cartesian coordinates of calculated structures ([TXT](#))

■ AUTHOR INFORMATION

Corresponding Authors

*martin.srnec@jh-inst.cas.cz

*edward.solomon@stanford.edu

ORCID

Martin Srnec: [0000-0001-5118-141X](https://orcid.org/0000-0001-5118-141X)

Notes

The authors declare no competing financial interest.

■ ACKNOWLEDGMENTS

This project was supported by the National Institute of General Medical Sciences of the National Institutes of Health under

award number R01GM040392 and by the Grant Agency of the Czech Republic (Grant no. 15-10279Y). M.S. is also grateful to the Czech Academy of Sciences for the Purkyně fellowship.

■ REFERENCES

- (1) Solomon, E. I.; Brunold, T. C.; Davis, M. I.; Kemsley, J. N.; Lee, S. K.; Lehnert, N.; Neese, F.; Skulan, A. J.; Yang, Y. S.; Zhou, J. *Chem. Rev.* **2000**, *100*, 235–350.
- (2) Rokob, T. A.; Chalupský, J.; Bím, D.; Andrikopoulos, P. C.; Srnec, M.; Rulišek, L. *JBIC, J. Biol. Inorg. Chem.* **2016**, *21*, 619–644.
- (3) Vaillancourt, F. H.; Yin, J.; Walsh, C. T. *Proc. Natl. Acad. Sci. U. S. A.* **2005**, *102*, 10111–10116.
- (4) Blasiak, L. C.; Vaillancourt, F. H.; Walsh, C. T.; Drennan, C. L. *Nature* **2006**, *440*, 368–371.
- (5) Matthews, M. L.; Krest, C. M.; Barr, E. W.; Vaillancourt, F. H.; Walsh, C. T.; Green, M. T.; Krebs, C.; Bollinger, J. M., Jr. *Biochemistry* **2009**, *48*, 4331–4343.
- (6) Wong, S. D.; Srnec, M.; Matthews, M. L.; Liu, L. V.; Kwak, Y.; Park, K.; Bell, C. B., III; Alp, E. E.; Zhao, J.; Yoda, Y.; Kitao, S.; Seto, M.; Krebs, C.; Bollinger, J. M., Jr.; Solomon, E. I. *Nature* **2013**, *499*, 320–323.
- (7) Mitchell, A. J.; Zhu, Q.; Maggiolo, A. O.; Ananth, N. R.; Hillwig, M. L.; Liu, X.; Boal, A. K. *Nat. Chem. Biol.* **2016**, *12*, 636–640.
- (8) Srnec, M.; Wong, S. D.; Matthews, M. L.; Krebs, C.; Bollinger, J. M., Jr.; Solomon, E. I. *J. Am. Chem. Soc.* **2016**, *138*, 5110–5122.
- (9) Matthews, M. L.; Neumann, C. S.; Miles, L. A.; Grove, T. L.; Booker, S. J.; Krebs, C.; Walsh, C. T.; Bollinger, J. M., Jr. *Proc. Natl. Acad. Sci. U. S. A.* **2009**, *106*, 17723–17728.
- (10) Matthews, M. L.; Chang, W. C.; Layne, A. P.; Miles, L. A.; Krebs, C.; Bollinger, J. M., Jr. *Nat. Chem. Biol.* **2014**, *10*, 209–215.
- (11) Martinie, R. J.; Livada, J.; Chang, W.; Green, M. T.; Krebs, C.; Bollinger, J. M., Jr.; Silakov, A. *J. Am. Chem. Soc.* **2015**, *137*, 6912–6919.
- (12) Pandian, S.; Vincent, M. A.; Hillier, I. H.; Burton, N. A. *Dalton Trans.* **2009**, 6201–6207.
- (13) Kulik, H. J.; Blasiak, L. C.; Marzari, N.; Drennan, C. L. *J. Am. Chem. Soc.* **2009**, *131*, 14426–14433.
- (14) Kulik, H. J.; Drennan, C. L. *J. Biol. Chem.* **2013**, *288*, 11233–11241.
- (15) Borowski, T.; Noack, H.; Radoń, M.; Zych, K.; Siegbahn, P. E. M. *J. Am. Chem. Soc.* **2010**, *132*, 12887–12898.
- (16) Huang, J.; Li, C.; Wang, B.; Sharon, D. A.; Wu, W.; Shaik, S. *ACS Catal.* **2016**, *6*, 2694–2704.
- (17) Frisch, M. J.; Trucks, G. W.; Schlegel, H. B.; Scuseria, G. E.; Robb, M. A.; Cheeseman, J. R.; Scalmani, G.; Barone, V.; Mennucci, B.; Petersson, G. A.; Nakatsuji, H.; Caricato, M.; Li, X.; Hratchian, H. P.; Izmaylov, A. F.; Bloino, J.; Zheng, G.; Sonnenberg, J. L.; Hada, M.; Ehara, M.; Toyota, K.; Fukuda, R.; Hasegawa, J.; Ishida, M.; Nakajima, T.; Honda, Y.; Kitao, O.; Nakai, H.; Vreven, T.; Montgomery, J. A., Jr.; Peralta, J. E.; Ogliaro, F.; Bearpark, M.; Heyd, J. J.; Brothers, E.; Kudin, K. N.; Staroverov, V. N.; Kobayashi, R.; Normand, J.; Raghavachari, K.; Rendell, A.; Burant, J. C.; Iyengar, S. S.; Tomasi, J.; Cossi, M.; Rega, N.; Millam, J. M.; Klene, M.; Knox, J. E.; Cross, J. B.; Bakken, V.; Adamo, C.; Jaramillo, J.; Gomperts, R.; Stratmann, R. E.; Yazyev, O.; Austin, A. J.; Cammi, R.; Pomelli, C.; Ochterski, J. W.; Martin, R. L.; Morokuma, K.; Zakrzewski, V. G.; Voth, G. A.; Salvador, P.; Dannenberg, J. J.; Dapprich, S.; Daniels, A. D.; Farkas, Ö.; Foresman, J. B.; Ortiz, J. V.; Cioslowski, J.; Fox, D. J. *Gaussian G09*, revision D.01; Gaussian, Inc.: Wallingford, CT, 2009.
- (18) Becke, A. D. *Phys. Rev. A: At., Mol., Opt. Phys.* **1988**, *38*, 3098–3100.
- (19) Grimme, S.; Antony, J.; Ehrlich, S.; Krieg, H. *J. Chem. Phys.* **2010**, *132*, 154104.
- (20) Frequency calculations were performed on top of the optimized cluster models of SyrB2 that include seven frozen atoms (shown in Figure S1A). Within this approach, 21 degrees of freedom associated with the frozen atoms are projected out from the Hessian. This ensures that all structures (belonging to one catalytic cycle) have the same number of vibrational frequencies, among which there is no or one imaginary frequency depending on whether a minimum or transition

state is optimized. Note that ZPVE and other entropic/thermal corrections to Gibbs free energies are considered as crude approximations.

(21) Kaduk, B.; Kowalczyk, T.; Van Voorhis, T. *Chem. Rev.* **2012**, *112*, 321–370.

(22) Valiev, M.; Bylaska, E. J.; Govind, N.; Kowalski, K.; Straatsma, T. P.; van Dam, H. J. J.; Wang, D.; Nieplocha, J.; Apra, E.; Windus, T. L.; de Jong, W. A. *Comput. Phys. Commun.* **2010**, *181*, 1477–1489.

(23) CRC Handbook of Chemistry and Physics, 97th ed.; Haynes, W. M., Ed.; Taylor & Francis Group, LLC: UK, 2016.

(24) (a) Marcus, R. A. *J. Phys. Chem.* **1968**, *72*, 891–899. (b) Gilmore, K.; Alabugin, I. V. *Chem. Rev.* **2011**, *111*, 6513–6556.

(25) Puri, M.; Biswas, A. N.; Fan, R.; Guo, Y.; Que, L., Jr. *J. Am. Chem. Soc.* **2016**, *138*, 2484–2487.

(26) Cho, K.-B.; Wu, X.; Lee, Y.-M.; Kwon, Y. H.; Shaik, S.; Nam, W. *J. Am. Chem. Soc.* **2012**, *134*, 20222–20225.

(27) Cho, K.-B.; Hirao, H.; Shaik, S.; Nam, W. *Chem. Soc. Rev.* **2016**, *45*, 1197–1210.